A Shallow-to-Deep Feature Fusion Network for VHR Remote Sensing Image Classification

Sicong Liu, *Senior Member, IEEE,* Yongjie Zheng, *Student Member, IEEE,* Qian Du, *Fellow, IEEE,* Lorenzo Bruzzone, *Fellow, IEEE,* Alim Samat, *Member, IEEE,* Xiaohua Tong, *Senior Member, IEEE,* Yanmin Jin, and Chao Wang

***Abstract*—With more detailed spatial information being represented in very-high-resolution (VHR) remote sensing images, stringent requirements are imposed on accurate image classification. Due to the diverse land-objects with intraclass variation and interclass similarity, efficient and fine classification of VHR images especially in complex scenes is challenging. Even for some popular deep learning (DL) frameworks, geometric details of land-object may be lost in deep feature levels, so it is difficult to maintain the highly-detailed spatial information (e.g., edges, small objects) only relying on the last high-level layer. Moreover, many of the newly developed DL methods require massive well-labeled samples, which inevitably deteriorates the model generalization ability under the few-shot learning. Therefore, in this paper, a lightweight shallow-to-deep feature fusion network (SDF^{2}N) is proposed for VHR image classification, where the traditional machine learning (ML) and DL schemes are integrated to learn rich and representative information to improve the classification accuracy. In particular, the shallow spectral-spatial features are first extracted, and then a novel triple-stage fusion (TSF) module is designed to learn the saliency and discriminative information at different levels for classification. The TSF module includes three feature fusion stages, i.e., low-level spectral-spatial feature fusion, middle-level multi-scale feature fusion, and high-level multi-layer feature fusion. The proposed SDF^{2}N takes advantages of the shallow-to-deep features, which can extract representative and complementary information of crossing layers. It is important to note that even with limited training samples, the SDF^{2}N still can achieve satisfying classification performance. Experimental results obtained on three real VHR remote sensing data sets including two multispectral and one airborne hyperspectral images covering complex urban scenarios confirm the effectiveness of the proposed approach compared with the state-of-the-art methods.**

***Index Terms*—very high resolution (VHR) image classification, spectral-spatial feature extraction, shallow-to-deep feature fusion, extended multi-attribute profiles (EMAP), squeeze-excitation (SE) attention mechanism.**

I. Introduction

THE rapid development of new generation Earth-Observation (EO) satellites allows the acquisition of an increasing number of high-resolution (HR) and very-high-resolution (VHR) remote sensing images. This results in VHR multispectral (VHR-MS) images with very high spatial resolution and HR hyperspectral (HR-HS) images with high spectral-spatial resolution, which makes it possible to analyze land surface objects at an unprecedented detailed scale [1], [2]. Accurate and robust identification of multi-class objects in VHR remote sensing images is of great significance in various applications [3], [4]. However, such high spatial and spectral resolutions lead to many issues and challenges in image processing and applications. For example, the limited number of spectral bands but over-rich spatial representation of objects in VHR-MS images; the rich but redundant spectral-spatial information in HR-HS images; and the difficult feature extraction for classification. Moreover, the lack of a sufficient number of training samples is the primary cause of low classification performance especially for complex scenarios (e.g., urban land-use) [5]–[8]. Therefore, it is still a very challenging task in real applications to obtain high quality and reliable semantic land-cover mapping results from VHR remote sensing images with a limited number of samples.

In the past decades, researchers have made great efforts to exploit effective spectral-spatial joint methods for VHR image classification [9]–[16]. According to the feature extraction and fusion strategies in the literature, such classification methods can be divided into two main groups based on the use of traditional machine learning (ML) and on the advanced deep learning (DL) models.

For traditional ML models, many spectral-spatial feature extraction and fusion approaches have been proposed to fully exploit the properties of VHR images, thus improving the classification performance. These approaches include filtering-based methods (e.g., Gabor filter [9], guided filter [10]), morphology-based methods [e.g., attribute profiles (AP) [17], extended attribute profiles (EAP) [18], and extended multi-attribute profiles (EMAP) [19]], sparse-based methods [12], [20], multiple kernel-based methods [13], [21], and other integrated learning strategies [22]. ML-based classification methods have clear advantages due to their high flexibility,

This work was supported in part by the National Key Research and Development Program of China under Grant 2018YFB0505000 and 2018YFB0505400, in part by the National Natural Science Foundation of China under Grant 42071324 and Grant 42001387, and in part by the Shanghai Rising-Star Program under Grant 21QA1409100. (*Corresponding authors: Xiaohua Tong, Yongjie Zheng*)

Sicong Liu, Yongjie Zheng, Xiaohua Tong, Yanmin Jin and Chao Wang are with the College of Surveying and Geoinformatics, Tongji University, Shanghai 200092, China (e-mail: sicong.liu@tongji.edu.cn; yongjie.Zheng@outlook.com; xhtong@tongji.edu.cn; jinyanmin@tongji.edu.cn; wangchao2019@tongji.edu.cn).

Qian Du is with the Department of Electrical and Computer Engineering, Mississippi State University, Starkville, MS 39762 USA (e-mail: du@ece.msstate.edu).

Lorenzo Bruzzone is with the Department of Information Engineering and Computer Science, University of Trento, 38123 Trento, Italy (e-mail: lorenzo.bruzzone@unitn.it).

Alim Samat is with the Xinjiang Institute of Ecology and Geography, Chinese Academy of Sciences, Ürümqi 830011, China (e-mail: alim.smt@gmail.com).

low time consumption, and low training data requirement, which lead to their successful application to VHR image classification [11]. The concepts of morphological profile (MP) and extended MP (EMP) to model the spatial information were presented in [23], [24]. As an extension of MP, AP was proposed in [17], which models the spatial information more precisely than MP since more attributes of the input image can be considered. In [25], the K-means and principal component analysis (PCA) were utilized to learn the spatial feature. Then, spectral-spatial features were generated for HS image classification by concatenating the spatial feature representations in all or some principal components (PCs). In [26], a spectral-spatial multiple kernel learning method was proposed for HS image classification. Unlike the direct stacking methods, it used the spectral-spatial weighted composite kernel structure to better integrate spectral-spatial information. However, the performances of these methods are still far to be satisfactory due to the limited handcrafted feature representation, sensitive parameter settings, and possible poor generalization abilities.

Thanks to the discriminative feature representations and end-to-end learning capabilities, recently many DL-based frameworks have achieved remarkable success in the remote sensing image classification [e.g., Convolutional Neural Networks (CNNs) [14], [27], Recurrent Neural Networks (RNNs) [15], [28], Generative Adversarial Networks (GANs) [16], [29], and hybrid networks [30]]. The existing DL-based methods are usually constructed with multiple layers, which consider the low-level features as the input and produce the output for the middle-level or high-level features. However, neurons and layers in different models have their unique connections, and the effective integration of spectral-spatial information is mainly achieved through the specific design of forward and backward response units. This fusion strategy is limited by the characteristics of the network, which result in a poor interpretability. Therefore, except the internal fusion within each unit or layer, external fusion operations including the concatenate (concat), add, multiply, and attention weighting mechanism operations are usually applied. For instance, in [31], a novel cross-resolution hidden layer feature fusion (CRHFF) approach was proposed for joint classification of multi-resolution MS and PAN images. Hence the latent information is extracted and fused according to an autoencoder like deep network. In [32], a novel fast dense spectral–spatial convolution network (FDSSC) was proposed based on 3-D densely connected structures for the accurate classification of HS image. In [33], a spectral–spatial unified network (SSUN) was developed to extract spatial and spectral features according to a multiscale CNN and a long short-term memory (LSTM) network, respectively, and then features were cascaded together for image classification. In [34], a spectral–spatial residual network (SSRN) was proposed for HS image classification to learn deep discriminative features from abundant spectral features and spatial contexts based on consecutive specific residual blocks. In addition to the above CNN-based frameworks, there are some other advanced frameworks such as Graph Convolutional Network (GCN) and Transformer. By considering the rich spectral-spatial information of HS images, in [35], a novel miniGCN was proposed to train large-scale graph networks in a minibatch fashion. In [36], a new transformer-based backbone network, named SpectralFormer, was proposed to extract more spectral information of HS images. Although these DL-based methods have shown promising progress in VHR remote sensing image classification, there are still some open issues that require further investigations. They consist in:

1) Most of spectral-spatial fusion deep networks are designed for HS image classification, only few studies in the literature focus on VHR-MS image classification, with the result and the model generalization remains poor when simultaneously considering the two tasks.
2) The spectral-spatial fusion frameworks on the one hand, often do not integrate multi-level features, thus they have shortcomings for accurately identifying the interior and edges of high-detailed objects. On the other hand, some existing fusion strategies are not able to properly utilize the shallow-to-deep features and the saliency information presented at different scales.
3) Most of DL-based networks require a large number of training samples to support an effective model learning. Thus, their accuracy and stability in the few-shot learning cases are relatively poor.

Inspired by the aforementioned classification methods and also motivated to overcome the existing open issues, in this paper, we propose a novel shallow-to-deep feature fusion network (named SDF^{2}N) for VHR remote sensing image classification. The main contributions of this network can be summarised as follows.

1) Based on the joint fusion of shallow spectral-spatial features and the corresponding deep multi-scale features, it is capable to better capture the detailed spectral-spatial and shallow-to-deep information. Accordingly, the classification performance of highly-detailed land-objects in VHR images is enhanced step by step by following a hierarchical feature fusion process.
2) A novel triple-stage fusion (TSF) strategy with three core feature fusion stages is designed. It can sequentially capture and fuse the specific discriminative and representative spectral-spatial features presented in VHR images at low, middle and high levels. Therefore, the identification ability especially for the edge details of complex objects or small objects is significantly improved.
3) Differently from other advanced DL-based methods, the proposed SDF^{2}N approach shows its stability and excellent classification performance especially in the small-sample cases, and is in general suitable for different types of VHR data sets such as MS, HS and unmanned aerial vehicle (UAV)-RGB camera images. This greatly increases the potential use of the proposed approach to deal with complex scenes in practical multi-sensor applications.

Experimental results obtained on three real VHR remote sensing data sets including two MS data sets and one HS data set confirmed the effectiveness of the proposed approach comparing with the state-of-the-art methods.

The reminder of this article is organized as follows. Section II briefly introduces the related work. The proposed SDF^{2}N approach is described in details in Section III. Experimental results and the related analysis are presented in Section IV. Finally, Section V draws the conclusions and provides future directions.

II. Related Work

Notations used in this paper are summarized in Table I.

A. Extended Morphological Profile (EMAP)

As one of the most popular shallow feature extraction techniques, the morphology-based methods are proven to be useful to enhance the classification performance on VHR images. The popular algorithms include MP [23], EMP [24], AP [17], EAP [18], and EMAP [19]. Their rigorous mathematical foundation and inherent ability to capture spectral-spatial information have led to the rapid development of ML-based feature extraction and fusion strategies. It is worth noting that they also have the advantage to be effective also with a limited number of training data [11]. Among them, the AP and its expansions, i.e., EAP and EMAP, are the most widely used approaches owning to the stronger capability to model local spatial context information [25].

Let $\boldsymbol{X} \in \mathbb{R}^{H\times W\times M}$ be a VHR image, where H, W, and M represent height, width, and the number of bands, respectively. Let ϕ_λ and γ_λ be the attribute thickening and attribute thinning, respectively. AP calculated on a given band $\boldsymbol{x}_m$ ($m \subseteq$[0, M]) of $\boldsymbol{X}$ can be defined as:

$$AP(\boldsymbol{x}_m) = \{\phi_{\lambda_N}(\boldsymbol{x}_m), ..., \phi_{\lambda_1}(\boldsymbol{x}_m), \boldsymbol{x}_m, \gamma_{\lambda_1}(\boldsymbol{x}_m), ..., \gamma_{\lambda_N}(\boldsymbol{x}_m)\} \tag{1}$$

where N is the number of attribute thinning and thickening operations.

As an extension of AP, the EAP is achieved by consecutively applying the thinning and thickening filters to the original spectral bands or on their PCs:

$$EAP(\boldsymbol{X}) = \{AP(\boldsymbol{x}_1), ..., AP(\boldsymbol{x}_M)\} \tag{2}$$

The EMAP is designed by stacking different types of EAP generated according to different attribute parameters [37], to comprehensively model complex objects in an image [11]. In this work, three attributes including area (a), diagonal box (db), and standard deviation (sd) are selected to generate the EMAP features, which can be formulated as:

$$EMAP(\boldsymbol{X}) = \{EAP_a(\boldsymbol{X}), EAP_{db}(\boldsymbol{X}), EAP_{sd}(\boldsymbol{X})\} \tag{3}$$

where the thresholds for the above attributes are a=150, db=50, and sd=20.

B. CNN

CNN is a feed-forward neural network containing at least one convolution layer. In the field of remote sensing image processing, it is popular for pixel-wise classification [38]. In general, four types of layers are included in a CNN architecture: (1) the convolution layer, (2) the pooling layer, (3) the batch normalization (BN) layer, and (4) the fully connected (FC) layer [39]. According to the processing dimensions, the convolution can be 1-D, 2-D, and 3-D. For the most common 2-D convolution, a 2-D kernel moves along the height and width directions of an image, which extracts deep features within a specified local neighborhood. In order to better model the spectral-spatial characteristics of VHR images, the 2-D convolution is selected as the base module in this work. The mathematical formulation of the 2-D convolution can be expressed as:

$$\boldsymbol{X}^{l+1} = F(\boldsymbol{X}^l) = f_\delta(\omega^l * (\boldsymbol{X}^l) + b^l) \tag{4}$$

where $\boldsymbol{X}^l$ represents the input feature maps of the lth convolution layer, $\boldsymbol{X}^{l+1}$ is the output feature maps of the lth layer [also the input set of the $(l+1)$th layer] [40], ω^l and b^l are the weights and bias of the lth layer, respectively, and f_δ represents the ReLU activation function.

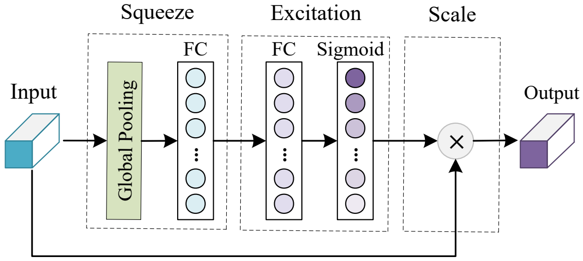

Fig. 1. SE Module [42].

C. Squeeze-Excitation (SE) Attention Mechanism

Attention has arguably become one of the most important concepts in the DL field. It is inspired by the biological systems of humans that tend to focus on distinctive parts when processing large amounts of information [41]. Among the popular attention mechanisms, one widely used module is the squeeze-excitation (SE) attention [42]. It can adaptively re-calibrate channel-wise feature responses by explicitly modeling interdependencies between channels [41]. In particular, SE module mainly uses global average-pooled features and FC features to compute channel-wise attention. As shown in Fig. 1, the structure of SE mainly consists of squeeze, excitation and scale steps [6], [43]. Let us assume $\boldsymbol{U} \in \mathbb{R}^{H\times W\times M}$ represent a given input feature vector.

1) Squeeze: The global average pooling (AvgPool) and FC operations are selected to build the squeeze transform F_{sq}, and the input feature vector $\boldsymbol{U}$ is squeezed into a global spatial 1-D feature vector (i.e., channel descriptor), which can be formulated as:

$$\boldsymbol{z}_m = F_{sq}(\boldsymbol{u}_m) = \frac{1}{H\times W}\sum_{i=1}^{H}\sum_{j=1}^{W}\boldsymbol{u}_m(i,j) \tag{5}$$

where $\boldsymbol{u}_m$ is the mth feature map of $\boldsymbol{U}$, i and j are the elements of the feature map, and $\boldsymbol{z}_m$ is the output of the squeeze operation.

TABLE I
NOTATIONS USED IN THIS PAPER

Symbol	Description	Symbol	Description
H	Height	W	Width
r	A reduction ratio	$W_1 \in \mathbb{R}^{\frac{W}{r} \times W}$	The FC layer for reducing dimension
$W_2 \in \mathbb{R}^{W \times \frac{W}{r}}$	The FC layer for infreasing dimension	M	Number of bands
$m \subseteq [0,\ M]$	-	B	Number of EMAP features
w	Window size	$\boldsymbol{X} \in \mathbb{R}^{H \times W \times M}$	VHR image
$\boldsymbol{X}' \in \mathbb{R}^{H \times W \times B}$	EMAP features	$\boldsymbol{I} \in \mathbb{R}^{w \times w \times B}$	Input features of TSF
$\boldsymbol{U} \in \mathbb{R}^{H \times W \times M}$	A given 3-D feature vector	N	Number of attribute operations
$\boldsymbol{x}_m$	The mth feature of $\boldsymbol{X}$	$\boldsymbol{z}_m$	Output of the squeeze operation
$\boldsymbol{u}_m$	The mth feature of $\boldsymbol{U}$	$\widetilde{\boldsymbol{u}}_m$	Output feature of SE module
ϕ_λ	Attribute thickening operation	γ_λ	Attribute thinning operation
a	Area attribute	db	Diagonal box attribute
sd	Standard deviation attribute	l	Number of layers
ω	Weight	b	Bias
F	Convolution operation	F_{sq}	Squeeze transform
F_{ex}	Excitation transform	F_{sc}	Scale transform
f_δ	ReLU activation function	f_σ	Sigmoid function
(i, j)	Pixel location	$\boldsymbol{s}$	The weight calculated by SE module
$1 \leq d \leq 128$	The dth channel	$1 \leq k \leq w$	Local window size
$t \in R^d_{k,k}$	-	ϵ	A very small constant
$\boldsymbol{I}'$	A given output feature vector	C	Number of classes
$c \subseteq [0,\ C]$	-	$y \in \{1, 2, ..., C\}$	The category label of $\boldsymbol{I}'$
$\hat{y} \in \{1, 2, ..., C\}$	The predicted label of $\boldsymbol{I}'$	ω_c	The weight vector of cth class

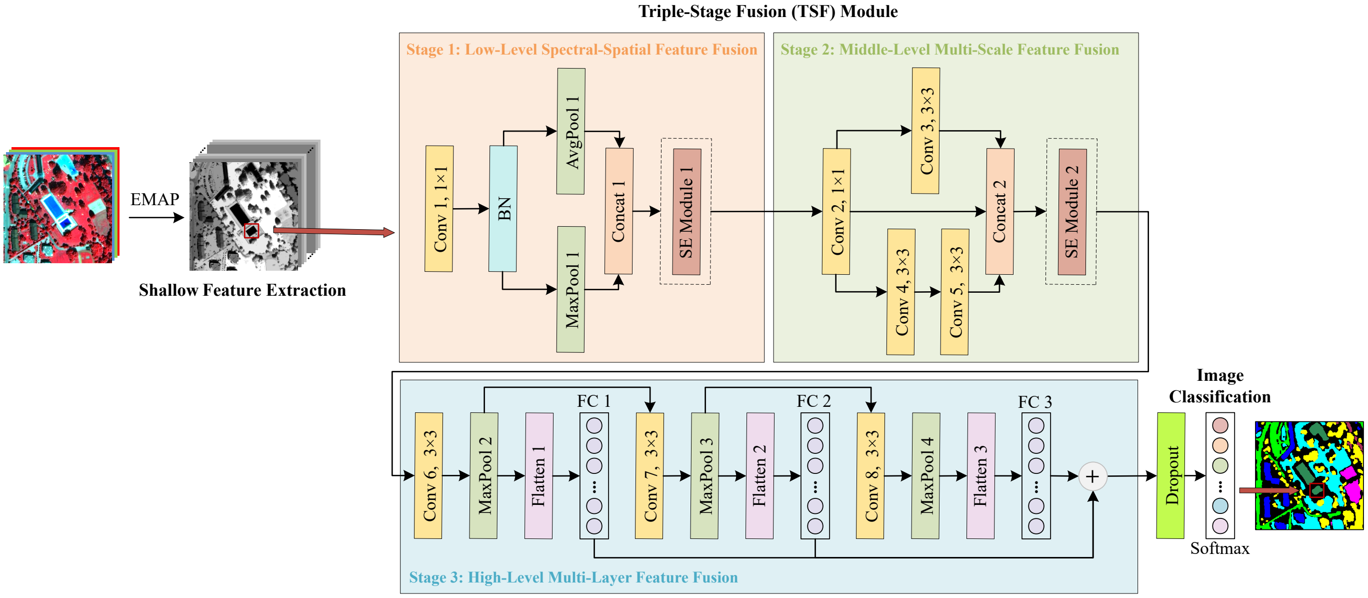

Fig. 2. Flowchart of the proposed SDF^{2}N for VHR image classification. It comprises shallow feature extraction, triple-stage fusion (TSF) and image classification three modules, where the TSF module consists of three sequential feature fusion stages: low-level spectral-spatial feature fusion, middle-level multi-scale feature fusion, and high-level multi-layer feature fusion.

2) Excitation: The excitation transform F_{ex} performs a nonlinear transformation on the squeezed result based on a FC layer, and compresses the weights of different features to 0-1 through the sigmoid function:

$$\boldsymbol{s} = F_{ex}(\boldsymbol{z}, W) = f_\sigma(W_2 f_\delta(W_1 \boldsymbol{z})) \tag{6}$$

where $W_1 \in \mathbb{R}^{\frac{W}{r} \times W}$ and $W_2 \in \mathbb{R}^{W \times \frac{W}{r}}$ are the FC layers for reducing and increasing dimension, respectively. r is a reduction ratio, $\boldsymbol{s}$ is the output of the excitation operation (which also can be seen as the weight vector), and f_σ represents the sigmoid function.

3) Scale: The scale transform F_{sc} is also called the reweight or feature recalibration. The previous output $\boldsymbol{s}$ is applied to weight the input feature set $\boldsymbol{U}$. So the final output $\widetilde{\boldsymbol{u}}_m$ can be obtained through the F_{sc} operation.

$$\widetilde{\boldsymbol{u}}_m = F_{sc}(\boldsymbol{u}_m, \boldsymbol{s}_m) = \boldsymbol{s}_m \boldsymbol{u}_m \tag{7}$$

III. Proposed SDF^{2}N

Fig. 2 illustrates the architecture of the proposed SDF^{2}N approach, which consists of three main parts: (1) shallow feature extraction; (2) triple-stage fusion (TSF) ; (3) image classification. In particular, a novel TSF strategy is designed to sequentially capture and fuse the shallow-to-deep features in VHR image at different levels. In particular, the rich shallow artificial spectral-spatial features are fused in stage 1 at low level, the multi-scale features are fused in stage 2 at middle level, and the multi-layer abstract and discriminative features are fused in stage 3 at high level. More details are provided as follows.

A. Shallow Feature Extraction

Considering that VHR images usually contain several broad spectral bands, EMAP can effectively capture spectral-spatial features in an unsupervised fashion, and then provide richer shallow features as the input of DL-based networks. Therefore, we firstly extracted the EMAP features from the original VHR image $\boldsymbol{X}$. Let $\boldsymbol{X}' \in \mathbb{R}^{H \times W \times B}$ be the new data, where B is the number of EMAP features (B is equal to $7M$ in this paper). A patch with a size of $w \times w$ is created as the feature region (around each pixel). Therefore, the actual size of the input data is $\boldsymbol{I} \in \mathbb{R}^{w \times w \times B}$.

B. Triple-Stage Fusion (TSF) Module

1) Stage 1 - Low-Level Spectral-Spatial Feature Fusion: The handcrafted EMAP features generated in the previous step contain rich spectral-spatial information but with high redundancy. Therefore, the first stage of the TSF module is designed to overcome the drawback so as to effectively fuse the spectral-spatial information in a compound set of discriminate features (see Fig. 2).

Table II lists the structure parameter settings in this stage. Specifically, a 1×1 convolution layer with 128 kernels is first employed to transform $\boldsymbol{I}$ into $F(\boldsymbol{I}) \in \mathbb{R}^{w \times w \times 128}$ for capturing the complex and learnable interactions of cross-channel information. Next, the BN is connected behind to avoid the gradient vanishing phenomenon. It can be formalized as:

$$\boldsymbol{I}^2 = F(\boldsymbol{I}^1) = f_\delta[\omega^1 * (\boldsymbol{I}^1) + b^1] \tag{8}$$

$$\boldsymbol{I}^3 = \mathrm{BN}(\boldsymbol{I}^2) = \frac{\boldsymbol{I}^2 - \mathrm{E}(\boldsymbol{I}^2)}{\sqrt{\mathrm{Var}(\boldsymbol{I}^2) + \epsilon}} \tag{9}$$

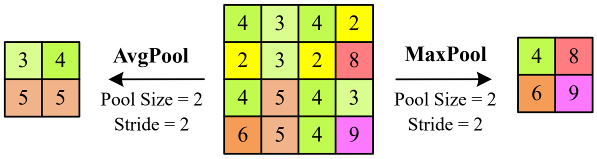

Fig. 3. The illustration of an example of the AvgPool and MaxPool operations.

TABLE II
NETWORK AND PARAMETERS SETTINGS IN THE STAGE 1 OF THE PROPOSED SDF^{2}N

Layers	Filter Size	Activation	Strides	Padding	Output Shape
Conv 1	128×1×1	ReLU	1	same	32×32×128
BN	/	/	/	/	32×32×128
AvgPool 1	2×2	/	2	valid	16×16×128
MaxPool 1	2×2	/	2	valid	16×16×128
Concat 1	/	/	/	/	16×16×256
SE Module 1	/	/	/	/	16×16×256

where $\boldsymbol{I}^1$ is equal to $\boldsymbol{I}$, $\mathrm{E}(\boldsymbol{I}^2)$ and $\mathrm{Var}(\boldsymbol{I}^2)$ are the expectation and variance function of $\boldsymbol{I}^2$, respectively, and ϵ is a very small constant value (i.e., $1e-5$) that maintain stability.

Then, two kinds of pooling layers, i.e., the global max pooling (MaxPool) and the AvgPool, are combined to obtain the texture detailed information and background information, respectively. This can also improve the representability of geometric details of complex objects. The pooling operations are illustrated in Fig. 3. Let the input feature maps of two pooling layers be $\boldsymbol{I}^3 \in \mathbb{R}^{w \times w \times 128}$. For each feature map $\boldsymbol{I}_d^3 \in \mathbb{R}^{w \times w}$, the MaxPool selects the maximum value, while the AvgPool calculates the average value of a specific area $R_{k,k}^d$ as its representation.

$$\boldsymbol{I}_t^4 = \mathrm{MaxPool}(\boldsymbol{I}^3) = \max_{t \in R_{k,k}^d} \boldsymbol{I}_t^3 \tag{10}$$

$$\boldsymbol{I}_t^5 = \mathrm{AvgPool}(\boldsymbol{I}^3) = \frac{1}{|R_{k,k}^d|} \sum_{t \in R_{k,k}^d} \boldsymbol{I}_t^3 \tag{11}$$

$$\boldsymbol{I}^6 = \mathrm{Concat}(\boldsymbol{I}^4, \boldsymbol{I}^5) = \left\{\boldsymbol{I}^4, \boldsymbol{I}^5\right\} \tag{12}$$

where $1 \leq d \leq 128$, and $1 \leq k \leq w$.

Finally, in order to improve the feature representation by modelling the interdependencies between different channels [43], the SE attention module is adopted to realize the weighted recalibration for low-level features.

$$\boldsymbol{I}^7 = \mathrm{SE}(\boldsymbol{I}^6) \tag{13}$$

2) Stage 2 - Middle-Level Multi-Scale Feature Fusion: After fusing of the spectral-spatial information in the previous stage, stage 2 aims to generate and fuse the middle-level multi-scale features. Filters are pivotal for the convolution operation in CNN [44]. The larger a scale filter, the larger the receptive field and stronger semantic representation (see Fig. 4). For complex image objects, the joint use of different scales can better retain the discriminant information. Therefore, in this stage, two types of filters (1×1 and 3×3) are used to construct a multi-receptive field feature learning mechanism, i.e., 1×1: $\boldsymbol{I}^8 = F(\boldsymbol{I}^7)$, 3×3: $\boldsymbol{I}^9 = F(\boldsymbol{I}^8)$, and $5 \times$

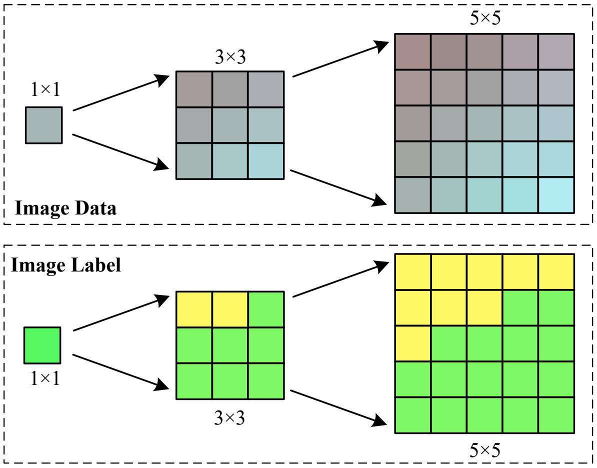

Fig. 4. Illustration of multi-receptive fields.

TABLE III
NETWORK AND PARAMETERS SETTINGS IN THE STAGE 2 OF THE PROPOSED SDF^{2}N

Layers	Filter Size	Activation	Strides	Padding	Output Shape
Conv 2	128×1×1	ReLU	1	same	16×16×128
Conv 3	128×3×3	ReLU	1	same	16×16×128
Conv 4	128×3×3	ReLU	1	same	16×16×128
Conv 5	128×3×3	ReLU	1	same	16×16×128
Concat 2	/	/	/	/	16×16×384
SE Module 2	/	/	/	/	16×16×384

5: $\boldsymbol{I}^{10} = F(F(\boldsymbol{I}^{8}))$. Due to the fact that larger receptive results in weaker spatial geometric features but requires more parameters, two 3 × 3 convolution layers are used in this work instead of the 5 × 5 convolution. This reduces the number of parameters, and increases the nonlinear expression ability. Finally, the same as in stage 1, the concatenation operation and SE module are used to further fuse the generated multi-scale features as

$$\boldsymbol{I}^{11} = \mathrm{Concat}(\boldsymbol{I}^{8}, \boldsymbol{I}^{9}, \boldsymbol{I}^{10}) \tag{14}$$

$$\boldsymbol{I}^{12} = \mathrm{SE}(\boldsymbol{I}^{11}) \tag{15}$$

3) Stage 3 - High-Level Multi-Layer Feature Fusion: In this stage, inspired by the classic VGG [45] and SSUN frameworks [33], middle-level features go through three pairs of convolution and pooling layers to extract the discriminative and abstract high-level features in a hierarchical manner. In particular, three high-level feature extraction architectures, i.e., a 3 × 3 convolution layer with 128 kernels and the corresponding 2 × 2 MaxPool layer are firstly stacked layer-by-layer as follows:

$$\boldsymbol{I}^{l+1} = F(\boldsymbol{I}^{l}) \tag{16}$$

$$\boldsymbol{I}^{l+2} = \mathrm{MaxPool}(\boldsymbol{I}^{l+1}) \tag{17}$$

$$\boldsymbol{I}^{l+7} = \mathrm{Flatten}(\boldsymbol{I}^{l+2}) \tag{18}$$

$$\boldsymbol{I}^{l+8} = \mathrm{FC}(\boldsymbol{I}^{l+7}) \tag{19}$$

TABLE IV
NETWORK AND PARAMETERS SETTINGS IN THE STAGE 3 OF THE PROPOSED SDF^{2}N

Layers	Filter Size	Activation	Strides	Padding	Output Shape
Conv 6	128×3×3	ReLU	1	same	16×16×128
MaxPool 2	2×2	/	2	valid	8×8×128
Flatten 1	/	/	/	/	8192
FC 1	128	ReLU	/	/	128
Conv 7	128×3×3	ReLU	1	same	8×8×128
MaxPool 3	2×2	/	2	valid	4×4×128
Flatten 2	/	/	/	/	2048
FC 2	128	ReLU	/	/	128
Conv 8	128×3×3	ReLU	1	same	4×4×128
MaxPool 4	2×2	/	2	valid	2×2×128
Flatten 3	/	/	/	/	512
FC 3	128	ReLU	/	/	128
Add	/	/	/	/	128

where $l \in \{12, 14, 16\}$. Then three pairs of convolution and MaxPool layers are followed by a flatten layer and an FC layer.

Finally, three high-level FC vectors are fused according to the add operation. Therefore, after the above sequential fusion operations, the high-level information at different layers is acquired to further enhance the semantic representation ability for land-objects in VHR images and thus improve the classification performance:

$$\boldsymbol{I}^{25} = \mathrm{Add}(\boldsymbol{I}^{20}, \boldsymbol{I}^{22}, \boldsymbol{I}^{24}) \tag{20}$$

C. Image Classification

In the final classification step, the obtained high-level features are first fed to the dropout layer to randomly discard half of features, which can avoid over-fitting and enhance the stability and generalization ability of the model. After that, the representative and discriminative features are input into the FC layer with the Softmax classifier for classification, where the cross entropy is used as the loss function. For the given output feature vector $\boldsymbol{I}'$ and its category label $y \in \{1, 2, ..., C\}$, the probability distribution can be expressed:

$$\begin{aligned} P(y = c \mid \boldsymbol{I}') &= \mathrm{softmax}(\omega_c \boldsymbol{I}') \\ &= \frac{\exp(\omega_c \boldsymbol{I}')}{\sum_{c'=1}^{C} \exp(\omega_{c'} \boldsymbol{I}')} \end{aligned} \tag{21}$$

where ω_c is the weight vector of the cth class. The final decision function of the Softmax can be formulated as follows:

$$\begin{aligned} \hat{y} &= \arg\max_{c=1}^{C} P(y = c \mid \boldsymbol{I}') \\ &= \arg\max_{c=1}^{C} \omega_c \boldsymbol{I}' \end{aligned} \tag{22}$$

where $\hat{y}$ represents the predicted label of the feature vector $\boldsymbol{I}'$.

IV. EXPERIMENTAL RESULTS AND ANALYSIS

A. Description of Data Sets

Experiments were conducted on three real VHR remote sensing data sets, including two satellite MS images, and one airborne HS image.

This article has been accepted for publication in IEEE Transactions on Geoscience and Remote Sensing. This is the author's version which has not been fully edited and content may change prior to final publication. Citation information: DOI 10.1109/TGRS.2022.3179288

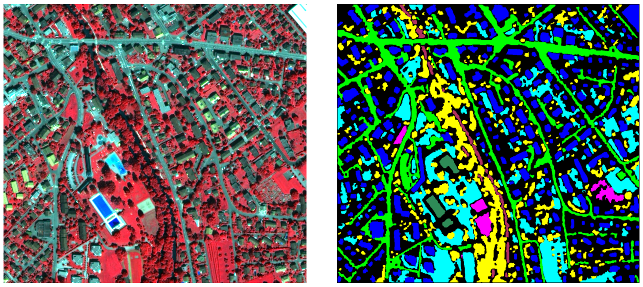

(a) (b)

Fig. 5. The ZH17 data set: (a) false color composite image (RGB: near-infrared, red and green bands) and (b) ground reference map.

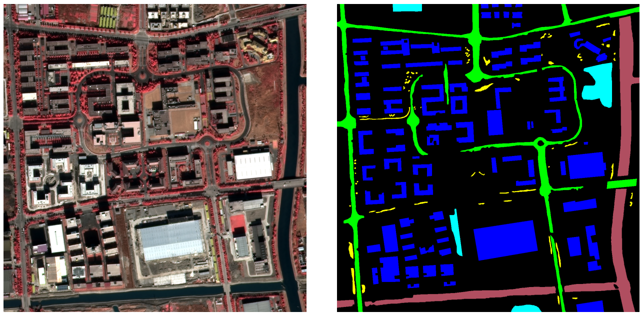

(a) (b)

Fig. 6. The SH data set: (a) false color composite image (RGB: near-infrared, red and green bands) and (b) ground reference map.

TABLE V
NUMBER OF SAMPLES OF THE ZH17 DATA SET

No.	Class Name	Color	Samples (pixel)
1	Roads	🟩	154786
2	Buildings	🟦	150627
3	Trees	🟨	111072
4	Grass	🟦	129125
5	Bare Soil	🟪	10619
6	Water	🟫	9040
7	Swimming Pools	🟩	6052

1) *Zurich 17 (ZH17):* The first data set was acquired by the QuickBird satellite over the urban area of the Zurich, Switzerland. The image contains 1025 × 1112 pixels and four spectral (blue, green, red and near-infrared) bands with an approximate resolution of 0.62 m after the pansharpening operation. The false color composite image and the corresponding ground reference map of the ZH17 data set are visualized in Fig. 5. As shown in Table V, in this scenario, there are seven land-cover classes including roads, buildings, trees, grass, bare soil, water, and swimming pools.

2) *Shanghai (SH):* The second data set was acquired by the Gaofen-2 satellite over the urban areas of Shanghai, China. The image contains 1220 × 1200 pixels and four spectral (blue, green, red and near-infrared) bands with a spatial resolution of 1 m after the pansharpening operation. Fig. 6 (a) and (b) present the false color composite image and the ground reference map, respectively. There exist five land-cover classes in the study area (i.e., buildings, roads, water, trees and grass). Detailed information on these classes is provided in Table VI.

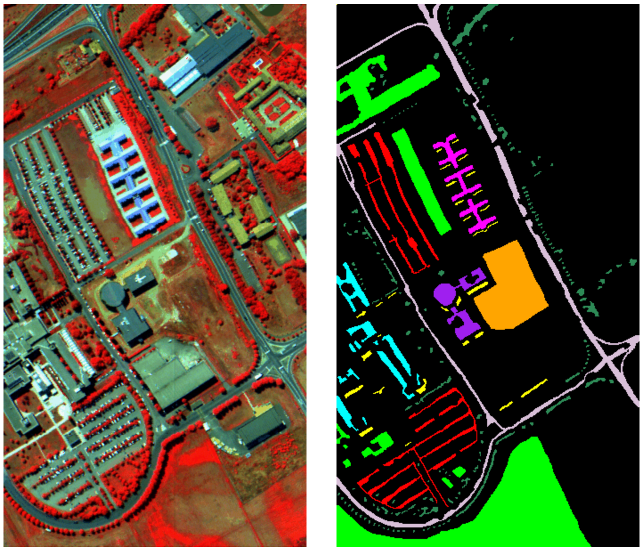

(a) (b)

Fig. 7. The UP data set: (a) false color composite image (RGB: bands 90, 50, and 10) and (b) ground reference map.

TABLE VI
NUMBER OF SAMPLES OF THE SH DATA SET

No.	Class Name	Color	Samples (pixel)
1	Buildings	🟦	195439
2	Roads	🟩	84444
3	Water	🟫	78043
4	Trees	🟨	11381
5	Grass	🟦	24868

TABLE VII
NUMBER OF SAMPLES OF THE UP DATA SET

No.	Class Name	Color	Samples (pixel)
1	Asphalt	⬜	6631
2	Meadows	🟩	18649
3	Gravel	🟦	2099
4	Trees	🟩	3064
5	Painted metal sheets	🟪	1345
6	Bare soil	🟧	5029
7	Bitumen	🟪	1330
8	Self-blocking bricks	🟥	3682
9	Shadows	🟨	947

3) *PaviaU (UP):* The third data set was acquired by the Reflective Optics Systems Imaging Spectrometer (ROSIS) sensor over the Pavia University, northern Italy. This image consists of 103 spectral bands (wavelength from 0.43 to 0.86 μm) having a size of 610 × 340 pixels and a spatial resolution of 1.3 m. In order to remove the redundancy in spectral bands, the PCA transformation was performed on the original full bands, where the first four PCs that retain 99% information of the input bands were kept for classification. Fig. 7 (a) and (b) present the false color composite image and the ground

reference map, respectively. There are nine complex classes in this data set, i.e., asphalt, meadows, gravel, trees, painted metal sheets, bare soil, bitumen, self-blocking bricks, and shadows (more information on classes can be seen in Table VII).

B. Parameter Settings

To demonstrate the effectiveness of the proposed SDF^{2}N approach, six reference methods were compared on the three considered data sets, including two traditional ML-based classification methods, i.e., support vector machine (SVM) and random forest (RF), and four state-of-the-art DL-based classification approaches, i.e., FDSSC [32], SSUN [33], SSRN [34], and SpectralFormer [36]. For the SVM classifier, the radial basis function (RBF) was selected as kernel function. For the RF classifier, the number of decision trees was set to 500. For three CNN-based reference networks FDSSC, SSUN and SSRN, the spatial window size of the input was set as 32 × 32, the batch size was set to 128, and the value of epochs was defined as 100. For the SpectralFormer, the values of patches, band-epochs, epochs were set to [7, 7, 480], [7, 3, 900], and [7, 7, 480] in ZH17, SH and UP three data sets, respectively. For the proposed SDF^{2}N, the Adam optimizer with a learning rate of 0.001 was used for model training. In addition, the parameter settings of the input window, batch and epoch were consistent with the aforementioned CNN-based reference methods. Finally, in order to keep consistency with the the proposed method, the EMAP features were also used as input to the six reference methods.

The DL-based methods (i.e., FDSSC, SSUN, SSRN, SpectralFormer, and SDF^{2}N) were implemented by TensorFlow or PyTorch on an NVIDIA P40 GPU with 24 GB memory. The ML-based methods (i.e., SVM and RF) were implemented by Matlab R2020b on a computer with Intel(R) Core(TM) i5-7300 CPU, RAM 8 GB.

To quantitatively evaluate the classification performance among all compared methods, different indices such as the overall accuracy (OA), the class accuracy (CA), the kappa coefficient (Kappa), and the computational time cost (T) were calculated. Final experimental results were obtained by repeat running ten times of each method with randomly generated training samples.

C. Experimental Results

In this section, we report the quantitative and qualitative analysis on the results obtained by the proposed approach and six reference methods on three VHR remote sensing data sets.

1) Results on the ZH17 data set: A detailed comparison of the classification performance of seven methods was done under different numbers of training samples, which were randomly selected as 1%, 2%, 3%, 4%, and 5% of samples for each class. Note that the randomization and classification were repeated ten times to assess average performance. The standard deviations (SD) of OA values are illustrated by the shaded areas in Fig. 8. In the figure, the red curve corresponds to the OA values obtained by the proposed SDF^{2}N method, which clearly shows higher values than the others with subtle fluctuation. Among four DL-based reference methods, FDSSC and SSUN outperformed SSRN and SpectralFormer. Unfortunately, the FDSSC performance fluctuated greatly under different random samplings. The SpectralFormer achieved the lowest accuracy but with stable performance. In addition, although the SVM and RF have the most stable performance, their accuracies are much lower than those of DL-based methods.

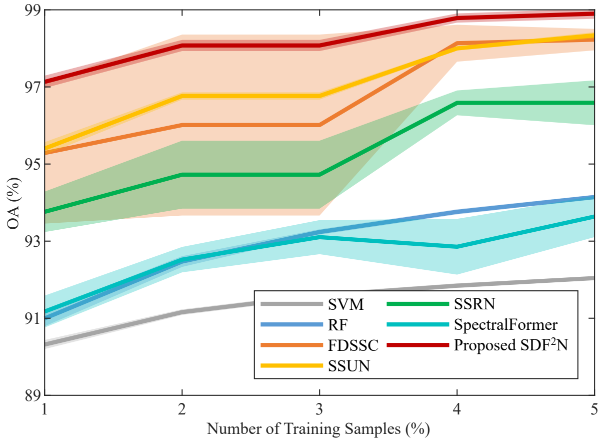

Fig. 8. OA results obtained by different methods with different numbers of randomly selected training samples (ZH17 data set). Each curve represents the average OA after ten-times random sampling, and the shaded area represents the SD of ten OA values.

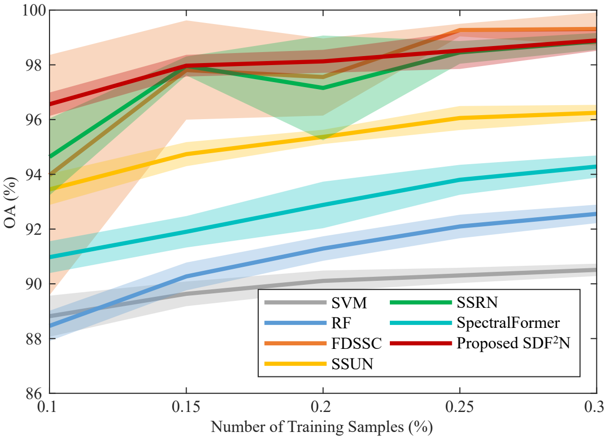

Fig. 9. OA results obtained by different methods with different numbers of randomly selected training samples (SH data set). Each curve represents the average OA after ten-times random sampling, and the shaded area represents the SD of ten OA values.

Table VIII summaries the classification accuracies obtained by different methods with 1% training samples. From the table, one can see that two ML-based methods obtained the worst average OA values among all considered methods (i.e., SVM: 90.32% and RF: 91.00%). Considering five DL-based methods, the proposed SDF^{2}N approach resulted in the highest classification accuracy (OA=97.13%), significantly outperforming four reference deep networks, i.e., FDSSC (95.29%), SSUN (95.40%), SSRN (93.76%), and SpectralFormer (91.17%). Moreover, the proposed SDF^{2}N approach produced a smallest SD value of OA (±0.16), indicating its stability.

The classification maps obtained by different methods under the first group of random samples are shown in Fig. 11. One

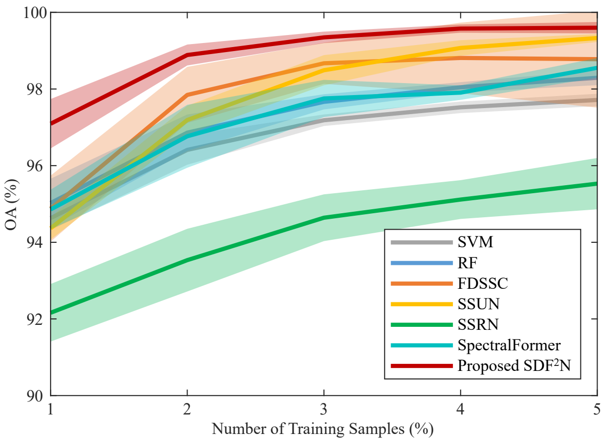

Fig. 10. OA results obtained by different methods with different numbers of randomly selected training samples (UP data set). Each curve represents the average OA under ten-times random sampling, and the shaded area represents the SD of ten OA values.

subset highlighted in Fig. 11 is further compared in Fig. 12. We can see that the classification maps proposed by SVM and RF present much noise, which leads to a decrease of OA values. Classification maps obtained by FDSSC [Fig. 12(c)], SSUN [Fig. 12(d)], SSRN [Fig. 12(e)], and SpectralFormer [Fig. 12(f)] contain some confusion between roads (in green) and trees (in yellow). Compared with the ground reference map [see Fig. 5(b)], the best classification map is obtained by using the proposed SDF^{2}N approach that resulted in an OA=97.14% [see Fig. 11(g) and Fig. 12(g)]. Most importantly, it is easy to observe that the proposed method alleviates the mis-classification pixels in the edges and interiors of adjacent objects (e.g., roads and trees), thus confirming its superiority on the other six compared methods.

2) Results on the SH data set: Fig. 9 illustrates the OA values obtained by different methods with a number of training samples increasing from 0.1% to 0.3% of total samples. In Fig. 9, among seven curves, the proposed SDF^{2}N approach (represented by the red curve) achieved higher OA values with more stable performance. Due to the fact that on the SH data set the land-cover types are relatively simple, all DL-based methods except the SpectralFormer obtained high classification accuracies with a limited number of training samples. The SpectralFormer may be more suitable for HS image classification owing to its strong capability in spectral feature learning, rather than the large-scene VHR image especially the one with very few broad spectral bands. In the meantime, performance with a small number of training samples demonstrates the stability of the advanced network. Therefore, although the accuracies of the FDSSC method are slightly higher than those of the SDF^{2}N in some conditions, its overall fluctuation is more significant than that of SDF^{2}N. In addition, comparing with other reference methods, SVM, RF and SpectralFormer resulted in more stable performances while their accuracies are quite lower.

Table IX reports the average classification accuracies and their SD values with 0.1% training samples. We can see that on this data set the obtained results are in line with the results of the previous data set. In particular, despite the lower SD values and computational time costs, SVM and RF resulted in the lowest average OA values which are equal to 88.82% and 88.46%, respectively. By taking advantages of powerful capability in extracting high-level semantic features, all five DL-based methods obtained high classification accuracies even in the few-shot learning cases. Among them, the proposed SDF^{2}N achieves the highest accuracy (i.e., OA=96.56%) with a smallest SD value (i.e., SD=0.43).

Fig. 13 shows the classification maps obtained by different methods by using the first group samples. Fig. 14 further illustrates the local classification results of the areas highlighted in Fig. 13. From Fig. 14, one can see that the proposed SDF^{2}N method obtained the fewest misclassified pixels [see Fig. 14(g)]. Compared with other six reference methods, the SDF^{2}N approach better models the object external edges and internal homogeneity of similar classes, thus reducing the misclassification errors, such as buildings (in blue) and roads (in green) classes, which are easy to be confused as shown in Fig. 13(g) and Fig. 14(g).

3) Results on the UP data set: Fig. 10 illustrates the accuracy obtained by different methods by using different numbers of samples. Compared with the previous two data sets, OA results better show the advantages of the proposed SDF^{2}N that provides the highest classification accuracy. On the contrary, the SSRN method achieved the lowest OA value. This may be due to the insufficient number of training samples in the model training process. In addition, the SpectralFormer obtained higher performance than in other data sets. This demonstrated it is more suitable for HS image classification with sufficient spectral information.

Table X presents the average classification accuracies of the seven methods with 1% training samples, which are consistent with the quantitative results of the previous two data sets. The proposed SDF^{2}N obtains the highest classification accuracy (OA=97.09%) and relatively small standard deviation (SD=0.64). In particular, the OA of the SDF^{2}N is higher of roughly 2%-5% than those of other methods and is obtained with a low computation cost (39.31 s).

Fig. 15 visualizes the classification maps of the first random sampling group obtained by different methods. In addition, subsets highlighted in the red rectangle in Fig. 15 are further compared in Fig. 16. It should be noted that the classification map obtained by the SDF^{2}N method presents more regular and correct classification results with less confusions among classes [see Fig. 15(g) and Fig. 16(g)]. It effectively reduces the misclassification especially for those complex objects with adjacent edges [e.g., asphalt (thistle) and trees (dark green)] and similar spectral characteristics [e.g., trees (dark green) and meadows (bright green)].

4) Ablation Study for the Proposed SDF^{2}N: To further validate the effectiveness of the proposed SDF^{2}N, a detailed ablation study was also made based on different combinations of the three fusion stages in the TSF module on the three data sets. As shown in Table XI, when only a single stage is considered (see rows 1-3), relatively poor performance are obtained as the multi-level features are not fused and utilized. In addition, although the combinations of two fusion stages

TABLE VIII
CLASSIFICATION ACCURACIES (%) OBTAINED BY DIFFERENT METHODS ON THE ZH17 DATA SET

Classes	SVM	RF	FDSSC	SSUN	SSRN	SpectralFormer	SDF^{2}N
Roads	89.62	89.54	97.11	95.29	95.97	87.76	97.48
Buildings	87.78	91.09	94.84	95.80	96.38	91.71	98.10
Trees	90.19	90.33	92.76	94.59	90.83	92.56	95.26
Grass	93.86	92.87	95.69	95.95	91.86	93.38	97.09
Bare soil	86.91	88.71	96.59	95.83	95.77	89.03	97.47
Railways	95.02	94.58	94.01	91.62	70.33	91.88	97.11
Swimming pools	97.04	96.59	96.88	96.35	97.72	95.41	98.80
OA	90.32	91.00	95.29	95.40	93.76	91.17	**97.13**
	±0.12	±0.20	±1.83	±0.17	±0.53	±0.41	±**0.16**
Kappa	87.38	88.26	93.85	94.01	91.86	88.50	96.26
	±0.16	±0.27	±2.40	±0.69	±0.69	±0.54	±0.21
T(s)	117.18	59.07	2606.99	300.80	1388.83	6545.93	485.59
	±6.07	±0.67	±41.62	±3.28	±13.91	±122.48	±11.93

TABLE IX
CLASSIFICATION ACCURACIES (%) OBTAINED BY DIFFERENT METHODS ON THE SH DATA SET

Classes	SVM	RF	FDSSC	SSUN	SSRN	SpectralFormer	SDF^{2}N
Buildings	85.51	88.77	92.54	93.42	94.25	90.35	96.15
Roads	84.72	77.75	98.52	89.77	97.41	82.66	94.07
water	99.55	99.91	96.70	99.04	98.66	99.05	99.34
Trees	86.12	74.64	54.14	72.15	43.85	93.46	96.78
Grass	96.29	92.81	99.46	98.39	98.93	97.68	99.43
OA	88.82	88.46	93.97	93.45	94.64	90.97	**96.56**
	±0.75	±0.55	±4.39	±0.57	±1.40	±0.58	±**0.43**
Kappa	83.43	82.67	91.16	90.16	91.97	86.48	94.84
	±1.09	±0.81	±5.97	±0.84	±2.07	±0.93	±0.63
T(s)	14.37	26.86	490.15	129.87	325.17	6399.58	165.48
	±0.90	±1.06	±22.10	±2.80	±25.52	±112.22	±6.69

TABLE X
CLASSIFICATION ACCURACIES (%) OBTAINED BY DIFFERENT METHODS ON THE UP DATA SET

Classes	SVM	RF	FDSSC	SSUN	SSRN	SpectralFormer	SDF^{2}N
Asphalt	93.85	95.06	98.67	96.53	96.04	91.66	98.73
Meadows	99.53	99.25	99.36	99.81	99.61	99.93	99.93
Gravel	65.31	68.23	94.11	76.45	94.17	72.35	90.40
Trees	90.17	86.64	66.29	89.79	39.32	92.28	91.72
Painted metal sheets	98.85	98.34	99.29	94.00	100.00	99.95	99.11
Bare soil	98.22	99.25	99.87	99.60	100.00	98.23	99.97
Bitumen	75.96	87.43	97.11	67.15	92.58	78.33	81.91
Self-blocking bricks	91.24	90.35	97.29	90.49	96.88	90.60	95.47
Shadows	97.29	99.81	28.98	52.62	13.18	90.29	71.66
OA	94.63	95.02	94.88	94.36	92.16	94.86	**97.09**
	±0.31	±0.63	±0.86	±0.29	±0.75	±0.52	±**0.64**
Kappa	92.85	93.38	93.19	92.48	89.55	93.17	96.14
	±0.42	±0.85	±1.15	±1.02	±1.02	±0.69	±0.86
T(s)	13.92	14.35	211.12	26.47	115.03	451.74	39.31
	±2.51	±0.25	±21.82	±0.74	±8.63	±11.66	±1.21

show better performance (see rows 4-6) than using a single stage, the proposed shallow-to-deep TSF structure (see row 7) resulted in the highest performance. This further demonstrates the effectiveness of the proposed SDF^{2}N that sequentially takes advantages of the three fusion stages to improve the classification performance in VHR images.

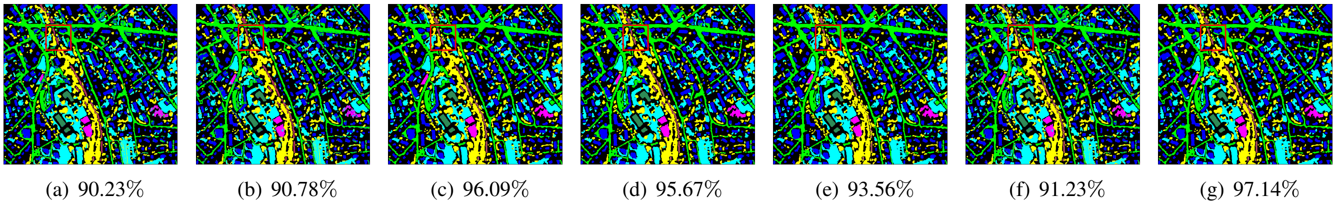
(a) 90.23% (b) 90.78% (c) 96.09% (d) 95.67% (e) 93.56% (f) 91.23% (g) 97.14%

Fig. 11. Classification maps obtained by different methods on the ZH17 data set. (a) SVM. (b) RF. (c) FDSSC. (d) SSUN. (e) SSRN. (f) SpectralFormer. (g) SDF^{2}N.

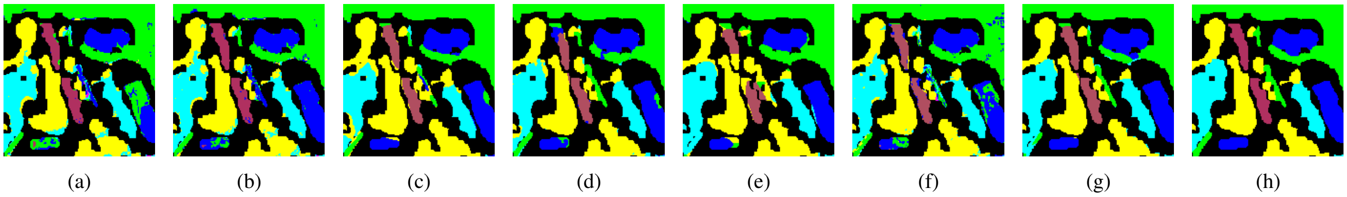
(a) (b) (c) (d) (e) (f) (g) (h)

Fig. 12. Classification maps obtained by different methods at a local subset on the ZH17 data set. (a) SVM. (b) RF. (c) FDSSC. (d) SSUN. (e) SSRN. (f) SpectralFormer. (g) SDF^{2}N. (h) Ground reference map.

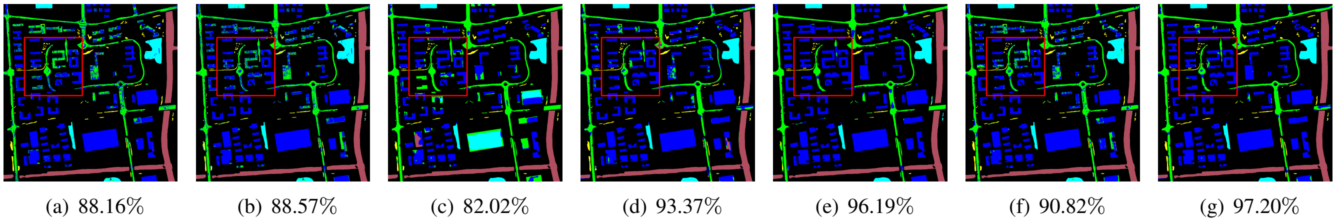
(a) 88.16% (b) 88.57% (c) 82.02% (d) 93.37% (e) 96.19% (f) 90.82% (g) 97.20%

Fig. 13. Classification maps obtained by different methods on the SH data set. (a) SVM. (b) RF. (c) FDSSC. (d) SSUN. (e) SSRN. (f) SpectralFormer. (g) SDF^{2}N.

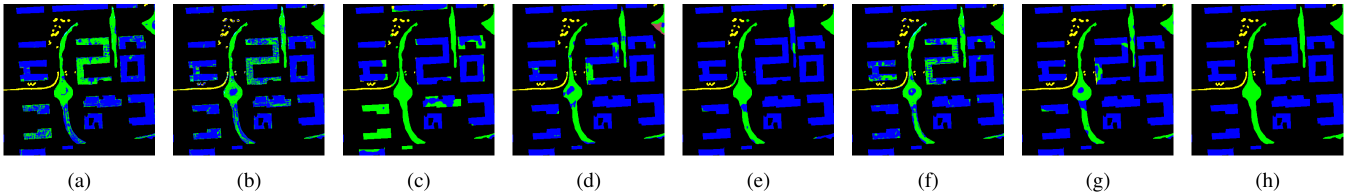
(a) (b) (c) (d) (e) (f) (g) (h)

Fig. 14. Classification maps obtained by different methods at a local subset on the SH data set. (a) SVM. (b) RF. (c) FDSSC. (d) SSUN. (e) SSRN. (f) SpectralFormer. (g) SDF^{2}N. (h) Ground reference map.

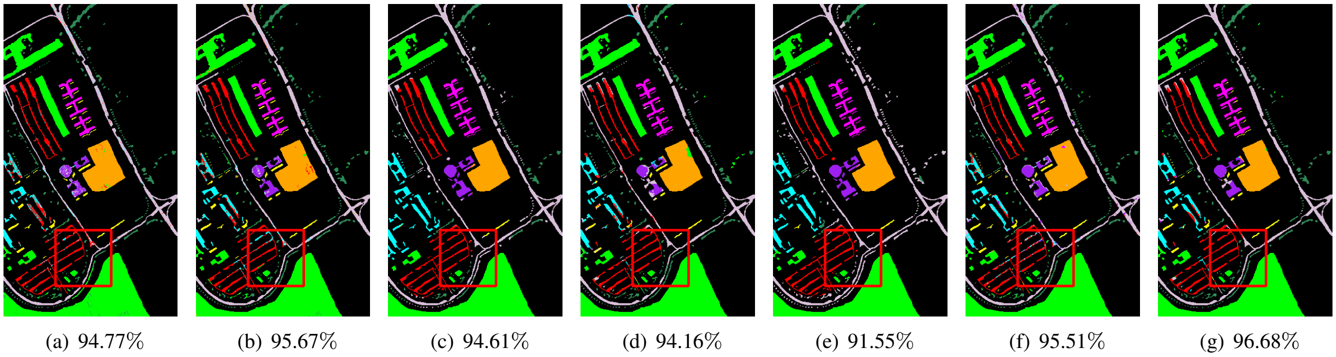
(a) 94.77% (b) 95.67% (c) 94.61% (d) 94.16% (e) 91.55% (f) 95.51% (g) 96.68%

Fig. 15. Classification maps obtained by different methods on the UP data set. (a) SVM. (b) RF. (c) FDSSC. (d) SSUN. (e) SSRN. (f) SpectralFormer. (g) SDF^{2}N.

V. Conclusion

In this paper, a novel shallow-to-deep feature fusion network (SDF^{2}N) has been proposed to hierarchically extract and fuse the saliency and discriminative features for VHR remote sensing image classification. Specifically, the SDF^{2}N contains three core feature fusion stages: (1) the low-level feature fusion stage, which is used to fuse the rich spectral-spatial features; (2) the middle-level feature fusion stage, which utilizes different size filters for integrating multi-scale spatial

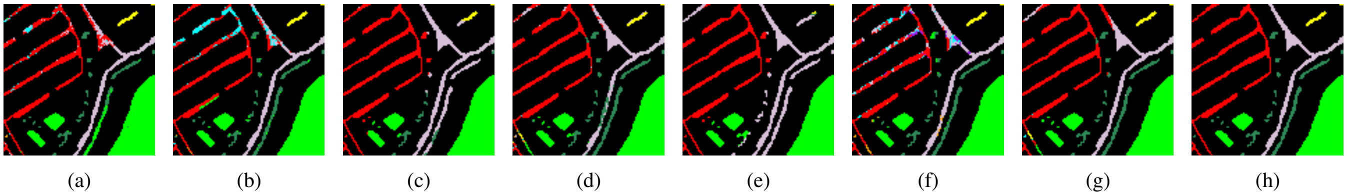

Fig. 16. Classification maps obtained by different methods at a local subset on the UP data set. (a) SVM. (b) RF. (c) FDSSC. (d) SSUN. (e) SSRN. (f) SpectralFormer. (g) SDF^{2}N. (h) Ground reference map.

TABLE XI
ABLATION STUDIES OF DIFFERENT FUSION STAGES

Combination strategies	OA(%)		
	ZH17	SH	UP
Stage 1	95.44 ±0.19	94.28 ±0.89	95.65 ±0.76
Stage 2	95.81 ±0.23	94.75 ±0.40	95.74 ±0.62
Stage 3	96.37 ±0.16	94.57 ±0.65	95.54 ±0.57
Stage 1&2	96.46 ±0.25	95.55 ±0.80	96.85 ±0.57
Stage 1&3	96.98 ±0.16	95.25 ±1.37	96.68 ±0.46
Stage 2&3	96.26 ±0.41	95.35 ±0.64	96.38 ±0.42
Stage 1&2&3	**97.13** **±0.16**	**96.56** **±0.43**	**97.09** **±0.64**

context information; and (3) the high-level feature fusion stage, which includes three hierarchical layers for learning abstract and discriminative information. Compared with six popular and state-of-the-art reference methods, experimental results obtained on three real VHR remote sensing data sets confirmed the effectiveness of the proposed SDF^{2}N approach. It effectively alleviates the inaccurate identification problems of complex objects especially in the high-detailed edges, and improves the classification accuracy. In addition, the proposed SDF^{2}N approach has the better model stability especially in the small-sample cases, where it is superior to the other considered reference state-of-the-art methods.

For future developments, we will explore more efficient shallow-to-deep feature fusion modules for a large complex scene classification in VHR satellite images.

Acknowledgment

The authors would like to thank Dr. Michele Volpi from Swiss Federal Institute of Technology Zurich for providing the QB data set, the China Centre for Resources Satellite Data and Application for providing the Gaofen-2 images, and also thank Prof. Paolo Gamba of the University of Pavia, for providing the University of Pavia hyperspectral data set.

References

[1] S. Liu, Y. Zheng, Q. Du, A. Samat, X. Tong, and M. Dalponte, “A novel feature fusion approach for VHR remote sensing image classification,” *IEEE Journal of Selected Topics in Applied Earth Observations and Remote Sensing*, vol. 14, pp. 464–473, 2021.

[2] S. Liu, D. Marinelli, L. Bruzzone, and F. Bovolo, “A review of change detection in multitemporal hyperspectral images: Current techniques, applications, and challenges,” *IEEE Geoscience and Remote Sensing Magazine*, vol. 7, no. 2, pp. 140–158, 2019.

[3] S. Liu, Q. Du, X. Tong, A. Samat, and L. Bruzzone, “Unsupervised change detection in multispectral remote sensing images via spectral-spatial band expansion,” *IEEE Journal of Selected Topics in Applied Earth Observations and Remote Sensing*, vol. 12, no. 9, pp. 3578–3587, 2019.

[4] F. Yang, W. Li, H. Hu, W. Li, and P. Wang, “Multi-scale feature integrated attention-based rotation network for object detection in VHR aerial images,” *Sensors*, vol. 20, p. 1686, 2020.

[5] J. R. Bergado, C. Persello, and A. Stein, “Recurrent multiresolution convolutional networks for vhr image classification,” *IEEE Transactions on Geoscience and Remote Sensing*, vol. 56, no. 11, pp. 6361–6374, 2018.

[6] Y. Tao, M. Xu, F. Zhang, B. Du, and L. Zhang, “Unsupervised-restricted deconvolutional neural network for very high resolution remote-sensing image classification,” *IEEE Transactions on Geoscience and Remote Sensing*, vol. 55, no. 12, pp. 6805–6823, 2017.

[7] S. Dong, Y. Zhuang, Z. Yang, L. Pang, H. Chen, and T. Long, “Land cover classification from VHR optical remote sensing images by feature ensemble deep learning network,” *IEEE Geoscience and Remote Sensing Letters*, vol. 17, no. 8, pp. 1396–1400, 2020.

[8] A. Samat, C. Persello, S. Liu, E. Li, Z. Miao, and J. Abuduwaili, “Classification of VHR multispectral images using extratrees and maximally stable extremal region-guided morphological profile,” *IEEE Journal of Selected Topics in Applied Earth Observations and Remote Sensing*, vol. 11, no. 9, pp. 3179–3195, 2018.

[9] X. Kang, C. Li, S. Li, and H. Lin, “Classification of hyperspectral images by gabor filtering based deep network,” *IEEE Journal of Selected Topics in Applied Earth Observations and Remote Sensing*, vol. 11, no. 4, pp. 1166–1178, 2018.

[10] S. Liu, Q. Hu, X. Tong, J. Xia, Q. Du, A. Samat, and X. Ma, “A multi-scale superpixel-guided filter feature extraction and selection approach for classification of very-high-resolution remotely sensed imagery,” *Remote Sensing*, vol. 12, p. 862, 2020.

[11] D. Maia, M.-T. Pham, E. Aptoula, F. Guiotte, and S. Lefèvre, “Classification of remote sensing data with morphological attribute profiles: A decade of advances,” *IEEE Geoscience and Remote Sensing Magazine*, vol. 9, pp. 43–71, 2021.

[12] E. Zhang, X. Zhang, H. Liu, and L. Jiao, “Fast multifeature joint sparse representation for hyperspectral image classification,” *IEEE Geoscience and Remote Sensing Letters*, vol. 12, no. 7, pp. 1397–1401, 2015.

[13] S. Niazmardi, A. Safari, and S. Homayouni, “A novel multiple kernel learning framework for multiple feature classification,” *IEEE Journal of Selected Topics in Applied Earth Observations and Remote Sensing*, vol. 10, no. 8, pp. 3734–3743, 2017.

[14] J. Wang, Y. Zheng, M. Wang, Q. Shen, and J. Huang, “Object-scale adaptive convolutional neural networks for high-spatial resolution remote sensing image classification,” *IEEE Journal of Selected Topics in Applied Earth Observations and Remote Sensing*, vol. 14, pp. 283–299, 2021.

[15] A. Ma, A. M. Filippi, Z. Wang, Z. Yin, D. Huo, X. Li, and B. Güneralp, “Fast sequential feature extraction for recurrent neural network-based hyperspectral image classification,” *IEEE Transactions on Geoscience and Remote Sensing*, vol. 59, no. 7, pp. 5920–5937, 2021.

[16] L. Zhu, Y. Chen, P. Ghamisi, and J. A. Benediktsson, “Generative adversarial networks for hyperspectral image classification,” *IEEE Transactions on Geoscience and Remote Sensing*, vol. 56, no. 9, pp. 5046–5063, 2018.

[17] M. Dalla Mura, J. A. Benediktsson, B. Waske, and L. Bruzzone, “Morphological attribute profiles for the analysis of very high resolution

images," *IEEE Transactions on Geoscience and Remote Sensing*, vol. 48, no. 10, pp. 3747–3762, 2010.

[18] M. Pedergnana, P. R. Marpu, M. Dalla Mura, J. A. Benediktsson, and L. Bruzzone, "Classification of remote sensing optical and LiDAR data using extended attribute profiles," *IEEE Journal of Selected Topics in Signal Processing*, vol. 6, no. 7, pp. 856–865, 2012.

[19] J. Li, H. Zhang, and L. Zhang, "Supervised segmentation of very high resolution images by the use of extended morphological attribute profiles and a sparse transform," *IEEE Geoscience and Remote Sensing Letters*, vol. 11, no. 8, pp. 1409–1413, 2014.

[20] L. Fang, S. Li, X. Kang, and J. A. Benediktsson, "Spectral–spatial classification of hyperspectral images with a superpixel-based discriminative sparse model," *IEEE Transactions on Geoscience and Remote Sensing*, vol. 53, no. 8, pp. 4186–4201, 2015.

[21] C. Zhao, X. Gao, Y. Wang, and J. Li, "Efficient multiple-feature learning-based hyperspectral image classification with limited training samples," *IEEE Transactions on Geoscience and Remote Sensing*, vol. 54, no. 7, pp. 4052–4062, 2016.

[22] S. Jia, J. Hu, Y. Xie, L. Shen, X. Jia, and Q. Li, "Gabor cube selection based multitask joint sparse representation for hyperspectral image classification," *IEEE Transactions on Geoscience and Remote Sensing*, vol. 54, no. 6, pp. 3174–3187, 2016.

[23] M. Pesaresi and J. Benediktsson, "A new approach for the morphological segmentation of high-resolution satellite imagery," *IEEE Transactions on Geoscience and Remote Sensing*, vol. 39, no. 2, pp. 309–320, 2001.

[24] J. Benediktsson, J. Palmason, and J. Sveinsson, "Classification of hyperspectral data from urban areas based on extended morphological profiles," *IEEE Transactions on Geoscience and Remote Sensing*, vol. 43, no. 3, pp. 480–491, 2005.

[25] L. Shu, K. McIsaac, and G. R. Osinski, "Learning spatial–spectral features for hyperspectral image classification," *IEEE Transactions on Geoscience and Remote Sensing*, vol. 56, no. 9, pp. 5138–5147, 2018.

[26] Y. Gu, K. Feng, and H. Wang, "Spatial-spectral multiple kernel learning for hyperspectral image classification," in *2013 5th Workshop on Hyperspectral Image and Signal Processing: Evolution in Remote Sensing (WHISPERS)*, 2013, pp. 1–4.

[27] S. K. Roy, G. Krishna, S. R. Dubey, and B. B. Chaudhuri, "HybridSN: Exploring 3-D–2-D CNN feature hierarchy for hyperspectral image classification," *IEEE Geoscience and Remote Sensing Letters*, vol. 17, no. 2, pp. 277–281, 2020.

[28] L. Mou, P. Ghamisi, and X. X. Zhu, "Deep recurrent neural networks for hyperspectral image classification," *IEEE Transactions on Geoscience and Remote Sensing*, vol. 55, no. 7, pp. 3639–3655, 2017.

[29] Z. Zhong, J. Li, D. A. Clausi, and A. Wong, "Generative adversarial networks and conditional random fields for hyperspectral image classification," *IEEE Transactions on Cybernetics*, vol. 50, no. 7, pp. 3318–3329, 2020.

[30] Y. Zheng, S. Liu, Q. Du, H. Zhao, X. Tong, and M. Dalponte, "A novel multitemporal deep fusion network (MDFN) for short-term multitemporal HR images classification," *IEEE Journal of Selected Topics in Applied Earth Observations and Remote Sensing*, vol. 14, pp. 10 691–10 704, 2021.

[31] S. Liu, H. Zhao, Q. Du, L. Bruzzone, A. Samat, and X. Tong, "Novel cross-resolution feature-level fusion for joint classification of multispectral and panchromatic remote sensing images," *IEEE Transactions on Geoscience and Remote Sensing*, vol. 60, pp. 1–14, 2022.

[32] W. Wang, S. Dou, Z. Jiang, and L. Sun, "A fast dense spectral–spatial convolution network framework for hyperspectral images classification," *Remote Sensing*, vol. 10, no. 7, 2018.

[33] Y. Xu, L. Zhang, B. Du, and F. Zhang, "Spectral–spatial unified networks for hyperspectral image classification," *IEEE Transactions on Geoscience and Remote Sensing*, vol. 56, no. 10, pp. 5893–5909, 2018.

[34] Z. Zhong, J. Li, Z. Luo, and M. Chapman, "Spectral–spatial residual network for hyperspectral image classification: A 3-D deep learning framework," *IEEE Transactions on Geoscience and Remote Sensing*, vol. 56, no. 2, pp. 847–858, 2018.

[35] D. Hong, L. Gao, J. Yao, B. Zhang, A. Plaza, and J. Chanussot, "Graph convolutional networks for hyperspectral image classification," *IEEE Transactions on Geoscience and Remote Sensing*, vol. 59, no. 7, pp. 5966–5978, 2021.

[36] D. Hong, Z. Han, J. Yao, L. Gao, B. Zhang, A. Plaza, and J. Chanussot, "Spectralformer: Rethinking hyperspectral image classification with transformers," *IEEE Transactions on Geoscience and Remote Sensing*, vol. 60, pp. 1–15, 2022.

[37] P. Ghamisi, J. A. Benediktsson, G. Cavallaro, and A. Plaza, "Automatic framework for spectral–spatial classification based on supervised feature extraction and morphological attribute profiles," *IEEE Journal of Selected Topics in Applied Earth Observations and Remote Sensing*, vol. 7, no. 6, pp. 2147–2160, 2014.

[38] Z. Zhang, L. Yang, and Y. Zheng, "Chapter 8-multimodal medical volumes translation and segmentation with generative adversarial network," in *Handbook of Medical Image Computing and Computer Assisted Intervention*, ser. The Elsevier and MICCAI Society Book Series, S. K. Zhou, D. Rueckert, and G. Fichtinger, Eds. Academic Press, 2020, pp. 183–204.

[39] S. Shajun Nisha and M. Nagoor Meeral, "Chapter 9-applications of deep learning in biomedical engineering," in *Handbook of Deep Learning in Biomedical Engineering*, V. E. Balas, B. K. Mishra, and R. Kumar, Eds. Academic Press, 2021, pp. 245–270.

[40] Z. Ge, G. Cao, X. Li, and P. Fu, "Hyperspectral image classification method based on 2D–3D CNN and multibranch feature fusion," *IEEE Journal of Selected Topics in Applied Earth Observations and Remote Sensing*, vol. 13, pp. 5776–5788, 2020.

[41] Z. Niu, G. Zhong, and H. Yu, "A review on the attention mechanism of deep learning," *Neurocomputing*, vol. 452, pp. 48–62, 2021.

[42] J. Hu, L. Shen, S. Albanie, G. Sun, and E. Wu, "Squeeze-and-excitation networks," *IEEE Transactions on Pattern Analysis and Machine Intelligence*, vol. 42, no. 8, pp. 2011–2023, 2020.

[43] A. Alshehri, Y. Bazi, N. Ammour, H. Almubarak, and N. Alajlan, "Deep attention neural network for multi-label classification in unmanned aerial vehicle imagery," *IEEE Access*, vol. 7, pp. 119 873–119 880, 2019.

[44] M. Liang, Z. Ren, J. Yang, W. Feng, and B. Li, "Identification of colon cancer using multi-scale feature fusion convolutional neural network based on shearlet transform," *IEEE Access*, vol. 8, pp. 208 969–208 977, 2020.

[45] K. Simonyan and A. Zisserman, "Very deep convolutional networks for large-scale image recognition," *Computer Science*, 2014.